ACS APPLIED MATERIALS & INTERFACES

www.acsami.org

Research Article

∑3 Twin Boundaries in $Gd_2Ti_2O_7$ Pyrochlore: Pathways for Oxygen Migration

Ashish Kumar Gupta, Gaurav Arora, Dilpuneet S. Aidhy, and Ritesh Sachan*

Cite This: *ACS Appl. Mater. Interfaces* 2020, 12, 45558–45563

Read Online

ACCESS | Metrics & More | Article Recommendations

ABSTRACT: Understanding the chemistry at twin boundaries (TB) is a well-recognized challenge, which could enable the capabilities to manipulate the functional properties in complex oxides. The study of this atomic imperfection becomes even more important, as the presence of twin boundaries has been widely observed in materials, regardless of the dimensionalities, due to the complexities in growth methods. In the present study, we provide atomic-scale insights into a $\sum 3(11\bar{1})\ \langle 1\bar{1}0\rangle$ twin boundary present in pyrochlore-structured $Gd_2Ti_2O_7$ using atomic-resolution electron microscopy and atomistic modeling. The formation of the observed TB occurs along $(11\bar{1})$ with a 71° angle between two symmetrically arranged crystals. We observe distortions (~3 to 5% strain) in the atomic structure at the TB with an increase in Gd−Gd (0.66 ± 0.03 nm) and Ti−Ti (0.65 ± 0.02 nm) bond lengths in the $(1\bar{1}0)$ plane, as compared to 0.63 nm in the ordered structure. Using atomistic modeling, we further calculate the oxygen migration barrier for vacancy hopping at 48f−48f sites in the pyrochlore structure, which is the primary diffusion pathway for fast oxygen transport. The mean migration barrier is lowered by ~25% to 0.9 eV at the TB as compared to 1.23 eV in the bulk, suggesting the ease in oxygen transport through the ∑3 twin boundaries. Overall, these results offer a critical understanding of the atomic arrangement at the twin boundaries in pyrochlores, leading to control of the interplay between defects and properties.

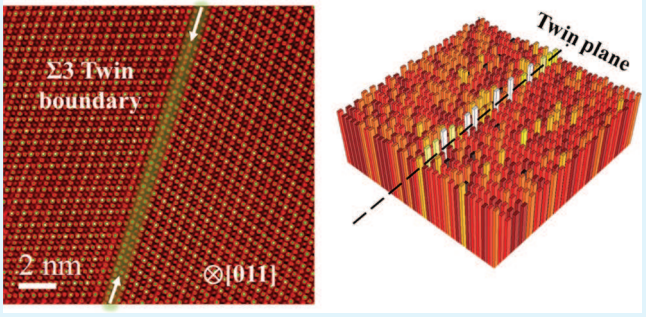

KEYWORDS: *pyrochlore, twin boundary, high-angle annular dark-field imaging, molecular dynamics oxygen migration barrier, ∑3 coherent grain boundaries, oxygen vacancies*

1. INTRODUCTION

Atomic-scale understanding of defects has always been a subject of interest for researchers in pursuit of modifying materials with improved functionalities. Over the years, significant attention has been given to such studies of twin boundary (TB) defects, which are considered as the key to unveiling various exciting properties, both in metals and in ceramics.[1−3] While TBs are desired in metals to induce superior mechanical properties with high strength and high ductility,[4,5] their introduction in ceramics is seen to overwhelmingly influence the properties for a variety of technological applications, including mechanical, magnetic, ferroelectric, and electronic and ionic transport.[2,6−9] TBs are the unique interfaces across that crystallographic arrangement of atoms mirroring each other. The importance of TBs is substantial due to their inevitable presence in virtually all of the materials, attributing to the complexities in the materials growth methods.[10] As the atomic arrangement at TBs strongly affects the overall properties of materials, understanding the atomic structure of these TBs is a stepping-stone toward forging structure−property correlations and further designing materials via defect/grain boundary engineering.

Particularly in ceramics, several studies have investigated the local atomic structure and coordination at the TBs to understand their effect on the corresponding properties. For example, the studies on TBs in yttria-stabilized zirconia were investigated using electron microscopy and first-principles calculations, which suggested the preferential segregation of yttrium atoms at TBs leading to the formation of a unique chemically ordered structure across the grain boundary.[11,12] Similarly, the interactions between Fe sublattice structures across the TB were studied in Fe_3O_4 magnetite thin films to understand its influence on the ferromagnetic coupling between two grains.[13] Atomic-scale elemental segregation studies at compositionally induced twin defects were also conducted in silver halides ($AgBr_xI_{1-x}$), which control the shape of the nanosized crystals, surface activity, and

Received: July 6, 2020
Accepted: September 11, 2020
Published: September 11, 2020

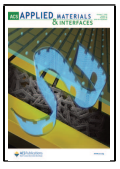

https://dx.doi.org/10.1021/acsami.0c12250
ACS Appl. Mater. Interfaces 2020, 12, 45558–45563

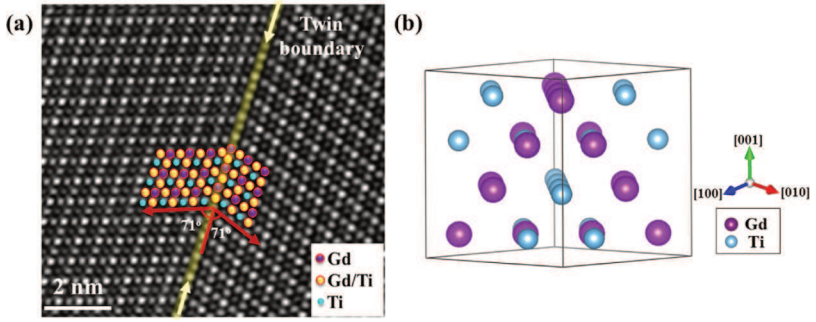

Figure 1. (a) HAADF image showing the $\sum 3\ (11\bar{1})[1\bar{1}0]$ twin boundary in $Gd_2Ti_2O_7$ and (b) atomic model depicting the atomic column of Gd and Ti. Oxygen atoms are not shown for clarity.

subsequently the photocatalytic properties.[14] Similar investigations in CdTe concluded segregation of Cl after Cl treatment at the coherent $\sum 3$ twin boundaries affecting the electrical activity for solar energy harvesting.[15] The defect energetics related to preferential vacancy site formation in symmetric $\sum 3$, $\sum 5$, and $\sum 13$ grain boundaries in $SrTiO_3$ and other perovskite oxides have also been analyzed, thereby establishing a correlation between the formation energy and the number of dangling bonds at the grain boundary (GB).[16−18] This observation was further correlated with the formation of electrical barriers invoked due to the change in the atomic coordination at the grain boundaries.[17] Overall, all of these studies demonstrate the critical impact of understanding the atomic structure at the grain boundaries for improving the design of materials.

In the case of fast ionic conduction, grain boundaries, surfaces, and interfaces play a pivotal role in addressing the transport limitations for emerging energy-related applications.[2,3] The presence of twin grain boundaries has been observed to increase the conductivity in YSZ due to yttrium segregation and resulting atomic rearrangement, attributed to an increase in the average concentration of oxygen vacancies.[19,20] A TB-assisted transport of lithium ions is also reported in single-crystalline SnO_2.[21] From the perspective of oxygen conductivity, pyrochlore-structured oxides ($A_2B_2O_7$) are significantly interesting materials[22−24] and are the focus of the present study. Due to the intrinsic possession of one ordered oxygen vacancy site (8b) per eight oxygen sites in the unit cell, the pyrochlore structure facilitates the fast diffusion of oxygen atoms and thus presents a huge opportunity in oxygen transport.[25] The application of $A_2B_2O_7$ oxides is broadened to their disordered defect-fluorite structure derivative, which is previously reported to have enhanced oxygen diffusivity due to a decrease in migration energy barrier caused by chemical randomness of A and B cations leading to unlocking of the oxygen vacancies in the unit cell.[26,27] Since the structural phase transformation from pyrochlore to defect-fluorite to achieve high oxygen diffusion is a challenge that requires extreme conditions,[28−30] the use of TB interfaces in pyrochlore oxides as pathways for oxygen transport is proposed as a novel alternative solution in this work. Here, we present an atomic-scale study of a $\sum 3$ twin boundary in pyrochlore $Gd_2Ti_2O_7$ and elucidate the associated oxygen migration properties. In this study, we use atomic-resolution imaging with a scanning transmission electron microscope (STEM) and correlative atomistic simulation to understand the structure at the TB. We further derive the correlation of the structure, bond lengths, and oxygen migration barriers, which layout the foundation to establish the twin boundaries as pathways for oxygen transport.

2. METHODOLOGY

2.1. Crystal Growth. Polycrystalline pyrochlore-structured $Gd_2Ti_2O_7$ was prepared by the conventional solid-state synthesis process. The starting materials were powders of Gd_2O_3 and TiO_2 (purity >99.9%, average particle size ∼5 μm). They were mixed in 1:2 stoichiometric ratio, followed by planetary ball milling for 12 h at room-temperature and 250 rpm. Tungsten carbide balls (2.5 mm) were used in a hardened steel vial. The homogenized composition was then hot-pressed at 1200 °C for 48 h. The as-processed samples were ∼10 mm in diameter after sintering, having a typical grain size of 50−80 μm.

2.2. STEM Characterization. The specimens for STEM investigations were prepared by drop-casting the ball-milled $Gd_2Ti_2O_7$ powder well mixed with methanol onto a lacey carbon TEM grid. The specimens were subsequently dried in air for 24 h. Prior to inserting into the microscope, the specimens were baked in vacuum for 8 h at 180 °C to remove moisture and carbonaceous hydrocarbons. The imaging in the [011] zone axis of $Gd_2Ti_2O_7$ from randomly oriented grains was performed by carefully identifying rightly oriented grains with the twin boundary. Microstructural analysis of specimens was performed on a fifth-order aberration-corrected scanning transmission electron microscope (STEM) (Nion UltraSTEM200), operating at 200 keV. Samples for STEM studies were prepared by the conventional thinning process, followed by ion milling in liquid nitrogen. High-angle annular dark-field imaging (HAADF) was done with an inner collection semi-angle of 65 mrad and an electron probe current of 28 ± 2 pA.

2.3. Computational Methods. The grain boundary (GB) structure is created using GB studio.[31] The structure is compared with the structure obtained from our STEM work. The GB supercell consists of a total of 8352 atoms. Atomic relaxation is performed using classical interatomic potential and the Large-scale Atomic/Molecular Massively Parallel Simulator (LAMMPS) code.[32] The interatomic potential for simulating $Gd_2Ti_2O_7$ is taken from Pirzada et al.[33] The Ewald method is used for electrostatic summation with a cutoff of 11 A°. The migration barriers are calculated using the nudged elastic band (NEB) method within the LAMMPS framework. The structure is relaxed using the steepest descent scheme as implemented in LAMMPS. Periodic boundary conditions are applied in all directions. After relaxing the structure in LAMMPS, the final dimensions of the GB structure are 49.57 A, 28.66 A, and 70.74 A° in *x*, *y*, and *z* directions,

https://dx.doi.org/10.1021/acsami.0c12250
ACS Appl. Mater. Interfaces 2020, 12, 45558−45563

respectively. Oxygen−oxygen bond length and oxygen vacancy migration barriers are calculated in the bulk and $\sum 3$ coherent twin grain boundary.

3. RESULTS AND DISCUSSION

Figure 1 shows the HAADF image of a $\sum 3$ twin boundary in $Gd_2Ti_2O_7$ crystal with the [011] zone axis. The TB in the $Gd_2Ti_2O_7$ crystal is in the $(11\bar{1})$ plane along the $[1\bar{1}0]$ direction. The angular rotation between the two crystals is measured to be 71 ± 0.1° around the twin plane $(11\bar{1})$. A schematic of the atomic model of $Gd_2Ti_2O_7$ oriented in $[1\bar{1}0]$ is overlaid on a region of crystals containing $\sum 3(11\bar{1})[1\bar{1}0]$ TB, illustrating the atomic arrangement along with an atomic model (Figure 1b). The crystal symmetry of $Gd_2Ti_2O_7$ grains and the rotation across the TB are demonstrated by fast Fourier transform (FFT) analysis, as shown in Figure 2. FFTs

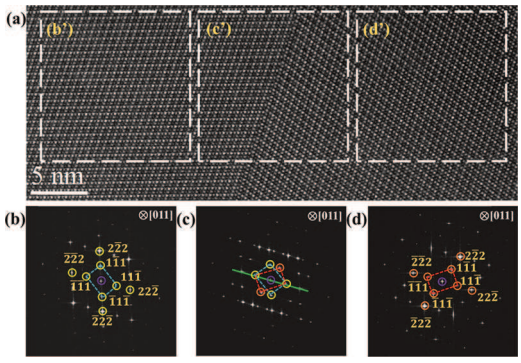

Figure 2. (a) HAADF image of a twin $\sum 3(11\bar{1})[1\bar{1}0]$ in the $Gd_2Ti_2O_7$ crystal, showing the crystallographic rotation across the twin boundary, and (b−d) diffraction patterns for the corresponding (b′−d′), while superimposition of diffraction spots is seen in (c).

(Figure 2b−d) were examined from different regions b′, c′, and d′, respectively, as marked in the HAADF image comprising two crystals of $Gd_2Ti_2O_7$ rotated by a TB (Figure 2a). While the FFTs in Figure 2b,d illustrate the diffraction spots corresponding to various crystallographic planes from individual $Gd_2Ti_2O_7$ crystals, the one in Figure 2c shows diffraction spots from both the crystals with some of the planes with mirror reflection. The appearance of indicated mirror reflections $(1\bar{1}1)$ and $(\bar{1}1\bar{1})$ is due to the crystallographic rotation across the twin plane. The plane of symmetry is depicted by a line (green color).

In various ceramic material systems, it is observed that the formation of $\sum 3$ twin boundaries exerts a rearrangement of atoms causing the events such as a change in bond lengths, segregation, and vacancy formation.[9,12,16,21] We investigate the atomic bond lengths between Gd−Gd (D_{Gd-Gd}) and Ti−Ti (D_{Ti-Ti}) atoms in the vicinity of TB, as shown in Figure 3. To determine the position of Gd and Ti atoms, we perform a script-based computational quantification, which estimates the atomic column position coordinates by identifying the atom intensities in the HAADF image.[34] This approach provides two-dimensional atom positions, thus the lattice spacing between various planes in the given HAADF image. The region of interest (ROI) for the atomic coordinate analysis is shown in Figure 3a. A magnified HAADF image of the atomic arrangement in $Gd_2Ti_2O_7$ in the [011] zone axis is shown in Figure 3b, where the measured atom-to-atom lengths D_{Gd-Gd} and D_{Ti-Ti} are defined. Using the described approach, the

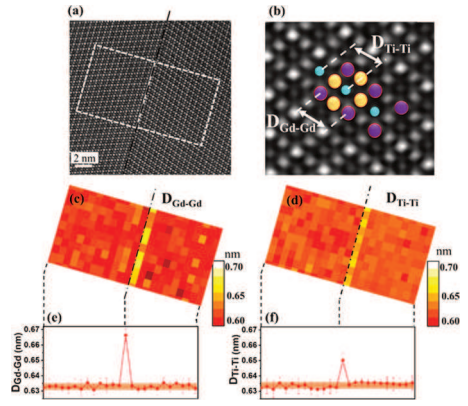

Figure 3. (a) HAADF image showing twin boundary; (b) magnified HAADF image of $Gd_2Ti_2O_7$ illustrating the defined Gd−Gd and Ti−Ti bond lengths; atomic bond length map of (c) D_{Gd-Gd} and (d) D_{Ti-Ti}, corresponding to ROI shown in (a); and average (e) D_{Gd-Gd} and (f) D_{Ti-Ti} for the same ROI. The analysis shows an increase in bond lengths at the twin boundary.

estimated atomic bond length maps for D_{Gd-Gd} and D_{Ti-Ti} are presented in Figure 3c,d, respectively. In an important observation, we determine an increase in D_{Gd-Gd} and D_{Ti-Ti} at the TB from 0.63 nm (i.e., in an ordered bulk structure) to 0.66 ± 0.03 and 0.65 ± 0.02 nm, respectively, which can be seen by the brighter intensity pixels at the TB in the maps. To further visualize this finding, plots elucidating the average D_{Gd-Gd} and D_{Ti-Ti} bond lengths across the TB in the ROI are shown in Figure 3e,f. These results clearly show an increase of bond lengths at the formed $\sum 3$ TB in $Gd_2Ti_2O_7$. These results are further used to determine the strain generated at the TB due to increasing lattice spacing, measured to be ∼5.15 and ∼3.05%, respectively, for Gd−Gd and Ti−Ti.

The results obtained from atomic position determination analysis are further confirmed by performing strain mapping using a geometric phase analysis (GPA) approach, as shown in Figure 4. The strain analysis is conducted over the HAADF

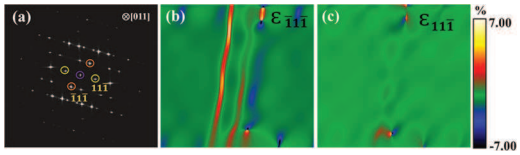

Figure 4. (a) FFT for the above HAADF image with a $\sum 3$ twin boundary, while marked diffraction spots are used for strain analysis. Images (b) and (c) show strain analysis in $(\bar{1}1\bar{1})$ and $(11\bar{1})$, respectively.

image (Figure 3a) using $(\bar{1}1\bar{1})$ and $(11\bar{1})$ diffraction spots, as shown in Figure 4a. The strain maps (Figure 4b,c) clearly show the presence of strain along the twin plane, while no/negligible strain is observed across it. The analysis further depicts ∼5.15% overall strain present at the TB, which is in qualitative agreement with the findings reported in Figure 3.

To further understand the reliable atomic arrangement and oxygen migration characteristics of the observed $\sum 3(11\bar{1})[1\bar{1}0]$ TB, atomistic simulations are conducted using interatomic potentials within the LAMMPS framework. Based on the inputs from our microscopic observations, a similar $\sum 3(11\bar{1})[1\bar{1}0]$ TB is reconstructed, as shown in Figure 5a. These boundaries are created while maintaining a periodic

https://dx.doi.org/10.1021/acsami.0c12250
ACS Appl. Mater. Interfaces 2020, 12, 45558−45563

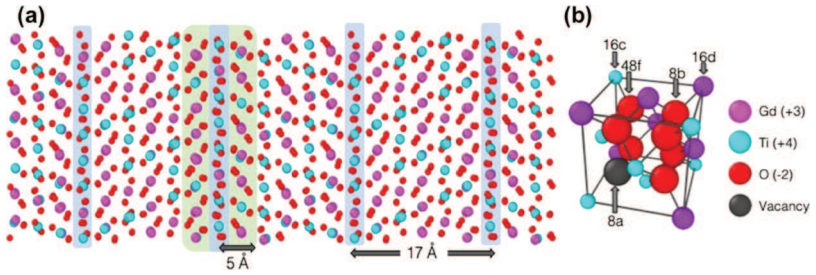

Figure 5. (a) Schematic of the ∑3 coherent twin GB structure used in this work. Highlighted areas represent the GB. Pink, cyan, and red spheres represent Gd, Ti, and O ions, respectively. Blue highlighted areas represent the actual GB, and the green highlighted area represents the area of the GB where the migration barrier calculations are performed. (b) Atomic structure of $Gd_2Ti_2O_7$ illustrating various lattice sites.

distance of 17 Å, as highlighted by the translucent blue rectangles. The green highlighted area represents the TB region where the migration barrier calculations are performed subsequently. Overall, the atomic relaxation is performed[25] over the atomic model to achieve a thermodynamically stable structure, representable for understanding the oxygen migration behavior.

In the case of pyrochlore structures, in general, oxygen migration is supported by the presence of an ordered oxygen vacancy at the 8b site. The rest of the anion sites 48f and 8a are occupied by oxygen atoms, whereas 16c and 16d cation sites in the unit cell are filled with Gd (A-type) and Ti (B-type) atoms, as shown in Figure 5b. In previous works,[27,33,35] it has been shown that the oxygen migration occurs via a vacancy hopping mechanism between two 48f and 48f anion positions in ⟨100⟩ directions in pyrochlore-structured $Gd_2Ti_2O_7$. Importantly, the activation energy of oxygen diffusion is highly influenced by the change in the bond lengths and thus the strain in the structure, like the present work at the TB.

As per literature, the 48f−48f bond length measured in the bulk structure is 2.65 A°.[35] In contrast to a single bond length in the bulk, due to the broken bonds, there is a wider distribution at the GB. The oxygen atoms within a distance of 5 A° on either side of the GB are taken into account, which results in a total of 1250 48f−48f bonds. These bonds are binned with a bin size of 0.05 Å, and the results are shown in Figure 6. The bulk 48f−48f bond length (2.65 Å) is plotted as a vertical line in Figure 6. We find that there is a large distribution of bond lengths at the GB. There are 19% bonds that are smaller and 81% bonds that are larger than the bulk bond length, as shown by green- and pink-shaded regions in Figure 6. Thus, we find that the bonds are generally stretched at the GB compared to the bulk, i.e., consistent with the experimental observation. We also calculate the grain boundary energy in the twinned $Gd_2Ti_2O_7$ system to be 0.785 J/m^2. It is important to note that the grain boundary energy value at the $\sum 3(11\bar{1})[1\bar{1}0]$ TB is relatively smaller than those of GBs formed by crystal misorientations due to atomic coherency at the TB.

In this work, we compare the migration barriers corresponding to 48f−48f migration between the bulk and at the TB. All 48f−48f oxygen−oxygen bond lengths and migration barriers are computed within a vicinity of 10 Å around the TB, as shown by the green highlighted region in Figure 7.

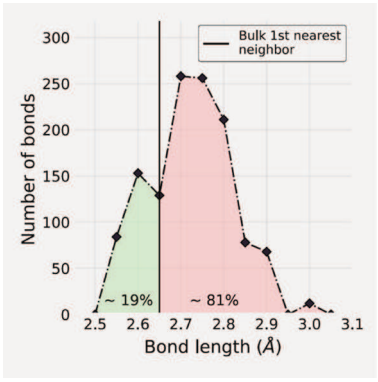

Figure 6. Variation in bond length obtained for the ions at the GB. Green and pink highlighted areas represent bond lengths having values lower and greater than the bulk first nearest-neighbor (NN) bond length, respectively. The bulk first NN bond length is shown by the black solid line.

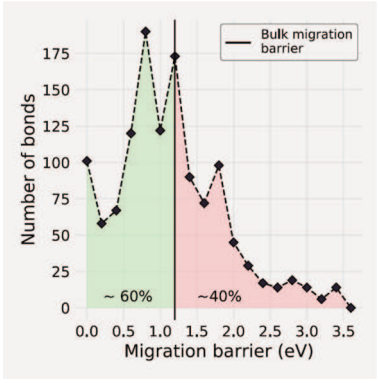

Figure 7. Variation obtained in the migration barrier for the GB structure. Green and pink highlighted areas represent the bonds that showed lower and higher migration barrier compared to the bulk. The bulk migration barrier is shown by the solid black line.

The bulk 48f−48f migration barrier is found to be 1.23 eV, which is in good agreement with the literature.[4,27,36] The migration barriers for all 1250 48f−48f bonds at the GB are shown in Figure 7. The barriers are binned with a bin size of 0.2 eV. The solid black line in Figure 7 represents the migration barrier corresponding to the bulk. The plot is divided into two parts represented by green and pink colors; the former represents barriers lower than the bulk, whereas the latter represents barriers higher than the bulk. We find that 60% barriers are lower than the bulk, bringing the mean migration barrier energy to be ∼0.9 eV, which is 25% lower than that in the bulk. Thus, while both high and low migration barriers are observed at the GB compared to the bulk, a significant portion of the barriers is lower, indicating a possibility of higher oxygen diffusion at the GB.

https://dx.doi.org/10.1021/acsami.0c12250
ACS Appl. Mater. Interfaces 2020, 12, 45558−45563

To put the oxygen migration barrier for the $\sum 3(11\bar{1})[1\bar{1}0]$ TBs in the perceptive, we collate the barrier energy for various pyrochlore oxides. The oxygen migration barrier is reported to be 1.23, 1.27, and 1.20 eV in $Gd_2Ti_2O_7$, $Y_2Ti_2O_7$, and $Er_2Ti_2O_7$, respectively.[37] Based on previous studies, it is also established that the atomic disordering in the pyrochlores lowers the oxygen migration barrier and thus enhances the oxygen diffusion. The atomic disordering directly depends on the defect energy, which decreases as a function of a decrease in the difference between ionic radii of A-site and B-site cations.[30,33,36,38,39] This is achieved in pyrochlores by substituting Ti at the B-site with Zr atoms with larger ionic radii. The oxygen migration barrier for $Gd_2Zr_2O_7$, $Sm_2Zr_2O_7$, and $Nd_2Ti_2O_7$ are theoretically determined to be in the range of 0.71−1.20 eV.[24,37,40,41] In addition, the alternative candidate oxides for oxygen conduction in solid-oxide fuel cells, i.e., CeO_2[42,43] and HfO_2,[44] show the barrier ranging ∼1.1 eV. Consistent with the findings of the present work, the formation of $\sum 3$ TBs in CeO_2 also shows the migration barrier ranging between 0.70 and 0.98 eV,[42] depending on the oxygen diffusion pathway, whereas those in monoclinic HfO_2 are estimated to be ∼0.57 eV.[44] Overall, this shows that the formation of $\sum 3$ TBs significantly improves the oxygen conduction as compared to the bulk pyrochlores and present a new perspective in designing grain boundaries for enhanced oxygen diffusion.

4. CONCLUSIONS

Using atomic-resolution electron microscopy and atomistic computational simulations, we presented atomic-scale insights into a $\sum 3(11\bar{1})[1\bar{1}0]$ twin boundary in pyrochlore-structured $Gd_2Ti_2O_7$. We investigated the twin boundary present between the crystals of $Gd_2Ti_2O_7$ with a crystallographic rotation of 71° and the $(11\bar{1})$ twin plane. With atomic column position analysis, we reveal that bond lengths of Gd−Gd and Ti−Ti are increased at the twin boundary along the $[1\bar{1}0]$ direction, leading to a higher strain of ∼5.15% at the twin boundary. Analogous to the experimental findings, we observe an average increase in the bond lengths between 48f and 48f anion sites (81% atomic bonds) at the twin boundary using computation in the LAMMPS framework. Since oxygen migration takes place in $Gd_2Ti_2O_7$ following the vacancy hopping between 48f and 48f sites, the change in the bond lengths is attributed to a lowering of the average migration barrier at the twin boundary. We estimate the bulk 48f−48f migration barrier to be 1.23 eV, while at the $\sum 3$ twin boundary, ∼0.9 eV. Overall, this study presents the interplay between the atomic arrangement at the $\sum 3$ twin boundary and the oxygen migration barrier in $Gd_2Ti_2O_7$ and establishes the twin boundaries as pathways for oxygen transport.

AUTHOR INFORMATION

Corresponding Author

Ritesh Sachan − *School of Mechanical and Aerospace Engineering, Oklahoma State University, Stillwater, Oklahoma 74078, United States;* orcid.org/0000-0002-3604-1467; Email: rsachan@okstate.edu

Authors

Ashish Kumar Gupta − *School of Mechanical and Aerospace Engineering, Oklahoma State University, Stillwater, Oklahoma 74078, United States*

Gaurav Arora − *Department of Mechanical Engineering, University of Wyoming, Laramie, Wyoming 82071, United States*

Dilpuneet S. Aidhy − *Department of Mechanical Engineering, University of Wyoming, Laramie, Wyoming 82071, United States*

Complete contact information is available at: https://pubs.acs.org/10.1021/acsami.0c12250

Author Contributions

A.K.G. and R.S. collected and analyzed STEM results. G.A. and D.S.A. performed atomistic simulations. A.K.G., G.A., D.S.A., and R.S. contributed to writing the manuscript. R.S. initiated and coordinated the research.

Notes

The authors declare no competing financial interest.

ACKNOWLEDGMENTS

R.S. acknowledges the support of faculty start-up funding at Oklahoma State University. The electron microscopic data acquisition in this research was conducted at the Center for Nanophase Materials Sciences, which is a DOE Office of Science User Facility. D.S.A. acknowledges support by the National Science Foundation under Grant No.1929112. G.A. and D.S.A. acknowledge the support of computational resources from Advanced Research Computing Center (ARCC) at the University of Wyoming.

REFERENCES

(1) Raabe, D.; Herbig, M.; Sandlöbes, S.; Li, Y.; Tytko, D.; Kuzmina, M.; Ponge, D.; Choi, P. P. Grain Boundary Segregation Engineering in Metallic Alloys: A Pathway to the Design of Interfaces. *Curr. Opin. Solid State Mater. Sci.* **2014**, *18*, 253−261.

(2) Frechero, M. A.; Rocci, M.; Sánchez-Santolino, G.; Kumar, A.; Salafranca, J.; Schmidt, R.; Díaz-Guillén, M. R.; Durá, O. J.; Rivera-Calzada, A.; Mishra, R.; et al. Paving the Way to Nanoionics: Atomic Origin of Barriers for Ionic Transport through Interfaces. *Sci. Rep.* **2015**, *5*, No. 17229.

(3) Vikrant, K. S. N.; García, R. E. Charged Grain Boundary Transitions in Ionic Ceramics for Energy Applications. *npj Comput. Mater.* **2019**, *5*, No. 24.

(4) George, E. P.; Raabe, D.; Ritchie, R. O. High-Entropy Alloys. *Nat. Rev. Mater.* **2019**, *4*, 515−534.

(5) Deng, Y.; Tasan, C. C.; Pradeep, K. G.; Springer, H.; Kostka, A.; Raabe, D. Design of a Twinning-Induced Plasticity High Entropy Alloy. *Acta Mater.* **2015**, *94*, 124−133.

(6) Li, X.; Yin, S.; Oh, S. H.; Gao, H. Hardening and Toughening Mechanisms in Nanotwinned Ceramics. *Scr. Mater.* **2017**, *133*, 105−112.

(7) Arlt, G. Twinning in Ferroelectric and Ferroelastic Ceramics: Stress Relief. *J. Mater. Sci.* **1990**, *25*, 2655−2666.

(8) Kobayashi, K.; Kimura, T.; Sawada, H.; Terakura, K.; Tokura, Y. Room-Temperature Magnetoresistance in Anoxide Materialwith Anordered Double-Perovskite Structure. *Nature* **1998**, *395*, 677−680.

(9) Feng, B.; Sugiyama, I.; Hojo, H.; Ohta, H.; Shibata, N.; Ikuhara, Y. Atomic Structures and Oxygen Dynamics of CeO_2 Grain Boundaries. *Sci. Rep.* **2016**, *6*, No. 20288.

(10) Carraro, G.; Gasparotto, A.; Maccato, C.; Bontempi, E.; Lebedev, O. I.; Sada, C.; Turner, S.; Van Tendeloo, G.; Barreca, D. Rational Synthesis of F-Doped Iron Oxides on Al2O3(0001) Single Crystals. *RSC Adv.* **2014**, *4*, 52140−52146.

(11) Feng, B.; Yokoi, T.; Kumamoto, A.; Yoshiya, M.; Ikuhara, Y.; Shibata, N. Atomically Ordered Solute Segregation Behaviour in an Oxide Grain Boundary. *Nat. Commun.* **2016**, *7*, No. 11079.

(12) Sánchez-Santolino, G.; Salafranca, J.; Pantelides, S. T.; Pennycook, S. J.; Leon, C.; Varela, M. Localization of Yttrium Segregation within YSZ Grain Boundary Dislocation Cores. *Phys. Status Solidi* **2019**, *215*, No. 1800349.
(13) Gilks, D.; McKenna, K. P.; Nedelkoski, Z.; Kuerbanjiang, B.; Matsuzaki, K.; Susaki, T.; Lari, L.; Kepaptsoglou, D.; Ramasse, Q.; Tear, S.; et al. Polar Spinel-Perovskite Interfaces: An Atomistic Study of Fe_3O_4 (111)/$SrTiO_3$ (111) Structure and Functionality. *Sci. Rep.* **2016**, *6*, No. 29724.
(14) Yin, B.; Huang, X.; Mishra, R.; Sadtler, B. Compositionally Induced Twin Defects Control the Shape of Ternary Silver Halide Nanocrystals. *Chem. Mater.* **2017**, *29*, 1014−1021.
(15) Li, C.; Poplawsky, J.; Yan, Y.; Pennycook, S. J. Understanding Individual Defects in CdTe Thin-Film Solar Cells via STEM: From Atomic Structure to Electrical Activity. *Mater. Sci. Semicond. Process.* **2017**, *65*, 64−76.
(16) Lee, H. S.; Mizoguchi, T.; Mistui, J.; Yamamoto, T.; Kang, S. J. L.; Ikuhara, Y. Defect Energetics in $SrTiO_3$ Symmetric Tilt Grain Boundaries. *Phys. Rev. B: Condens. Matter Mater. Phys.* **2011**, *83*, 2−11.
(17) Prabhumirashi, P.; Dravid, V. P.; Lupini, A. R.; Chisholm, M. F.; Pennycook, S. J. Atomic-Scale Manipulation of Potential Barriers at Grain Boundaries. *Appl. Phys. Lett.* **2005**, *87*, No. 121917.
(18) Imaeda, M.; Mizoguchi, T.; Sato, Y.; Lee, H.; Findlay, S. D.; Shibata, N.; Yamamoto, T.; Ikuhara, Y. Atomic Structure, Electronic Structure, and Defect Energetics in [001](310) $\sum$ 5 Grain Boundaries of $SrTiO_3$ and $BaTiO_3$. *Phys. Rev. B: Condens. Matter Mater. Phys* **2008**, *310*, No. 245320.
(19) Yoshida, H.; Yokoyama, K.; Shibata, N.; Ikuhara, Y.; Sakuma, T. High-Temperature Grain Boundary Sliding Behavior and Grain Boundary Energy in Cubic Zirconia Bicrystals. *Acta Mater.* **2004**, *52*, 2349−2357.
(20) An, J.; Park, J. S.; Koh, A. L.; Lee, H. B.; Jung, H. J.; Schoonman, J.; Sinclair, R.; Gur, T. M.; Prinz, F. B. Atomic Scale Verification of Oxide-Ion Vacancy Distribution near a Single Grain Boundary in YSZ. *Sci. Rep.* **2013**, *3*, No. 2680.
(21) Nie, A.; Gan, L. Y.; Cheng, Y.; Li, Q.; Yuan, Y.; Mashayek, F.; Wang, H.; Klie, R.; Schwingenschlogl, U.; Shahbazian-Yassar, R. Twin Boundary-Assisted Lithium-Ion Transport. *Nano Lett.* **2015**, *15*, 610−615.
(22) Takamura, H.; Tuller, H. L. Ionic Conductivity of Gd_2GaSbO_7−$Gd_2Zr_2O_7$ Solid Solutions with Structural Disorder. *Solid State Ionics* **2000**, *134*, 67−73.
(23) Tuller, H. L.; Moon, P. K. Fast Ion Conductors: Future Trends. *Mater. Sci. Eng. B* **1988**, *1*, 171−191.
(24) Moon, P. K.; Tuller, H. L. Ionic Conduction in the $Gd_2Ti_2O_7$−$Gd_2Zr_2O_7$ System. *Solid State Ionics* **1988**, *28*−*30*, 470−474.
(25) Sachan, R.; Chisholm, M. F.; Ou, X. I. N.; Zhang, Y.; Weber, W. J. Energetic Ion Irradiation-Induced Disordered Nanochannels for Fast Ion Conduction. *JOM* **2019**, *71*, 103−108.
(26) Sachan, R.; Cooper, V. R.; Liu, B.; Aidhy, D. S.; Voas, B. K.; Lang, M.; Ou, X.; Trautmann, C.; Zhang, Y.; Chisholm, M. F.; et al. Forging Fast Ion Conducting Nanochannels with Swift Heavy Ions: The Correlated Role of Local Electronic and Atomic Structure. *J. Phys. Chem. C* **2017**, *121*, 975−981.
(27) Aidhy, D. S.; Sachan, R.; Zarkadoula, E.; Pakarinen, O.; Chisholm, M. F.; Zhang, Y.; Weber, W. J. Fast Ion Conductivity in Strained Defect-Fluorite Structure Created by Ion Tracks in $Gd_2Ti_2O_7$. *Sci. Rep.* **2015**, *5*, No. 16297.
(28) Zhang, J.; Lang, M.; Ewing, R. C.; Devanathan, R.; Weber, W. J.; Toulemonde, M. Nanoscale Phase Transitions under Extreme Conditions within an Ion Track. *J. Mater. Res.* **2010**, *25*, 1344−1351.
(29) Lang, M.; Zhang, F.; Zhang, J.; Wang, J.; Schuster, B.; Trautmann, C.; Neumann, R.; Becker, U.; Ewing, R. C. Nanoscale Manipulation of the Properties of Solids at High Pressure with Relativistic Heavy Ions. *Nat. Mater.* **2009**, *8*, 793−797.
(30) Sachan, R.; Zarkadoula, E.; Lang, M.; Trautmann, C.; Zhang, Y.; Chisholm, M. F.; Weber, W. J. Insights on Dramatic Radial Fluctuations in Track Formation by Energetic Ions. *Sci. Rep.* **2016**, *6*, No. 27196.
(31) Ogawa, H. GBstudio: A Builder Software on Periodic Models of CSL Boundaries for Molecular Simulation. *Mater. Trans.* **2006**, *47*, 2706−2710.
(32) Plimpton, S. Fast Parallel Algorithms for Short-Range Molecular Dynamics. *J. Comput. Phys.* **1995**, *117*, 1−19.
(33) Pirzada, M.; Grimes, R. W.; Minervini, L.; Maguire, J. F.; Sickafus, K. E. Oxygen Migration in $A_2B_2O_7$ Pyrochlores. *Solid State Ionics* **2001**, *140*, 201−208.
(34) Zhang, Y.; Sachan, R.; Pakarinen, O. H.; Chisholm, M. F.; Liu, P.; Xue, H.; Weber, W. J. Ionization-Induced Annealing of Pre-Existing Defects in Silicon Carbide. *Nat Commun* **2015**, *6*, No. 8049.
(35) Gunn, D. S. D.; Allan, N. L.; Foxhall, H.; Harding, J. H.; Purton, J. A.; Smith, W.; Stein, M. J.; Todorov, I. T.; Travis, K. P. Novel Potentials for Modelling Defect Formation and Oxygen Vacancy Migration in $Gd_2Ti_2O_7$ and $Gd_2Zr_2O_7$ Pyrochlores. *J. Mater. Chem.* **2012**, *22*, 4675.
(36) Li, Y.; Kowalski, P. Energetics of Defects Formation and Oxygen Migration in Pyrochlore Compounds from First Principles Calculations. *J. Nucl. Mater.* **2018**, *505*, 255−261.
(37) Rushton, M. J. D.; Stanek, C. R.; Cleave, A. R.; Uberuaga, B. P.; Sickafus, K. E.; Grimes, R. W. Simulation of Defects and Defect Processes in Fluorite and Fluorite Related Oxides: Implications for Radiation Tolerance. *Nucl. Instrum. Methods Phys. Res., Sect. B* **2007**, *255*, 151−157.
(38) Sickafus, K. E.; Minervini, L.; Grimes, R. W.; Valdez, J. A.; Ishimaru, M.; Li, F.; McClellan, K. J.; Hartmann, T.; et al. Radiation Tolerance of Complex Oxides. *Science* **2000**, *289*, 748−751.
(39) Sachan, R.; Zarkadoula, E.; Ou, X.; Trautmann, C.; Zhang, Y.; Chisholm, M. F.; Weber, W. J. Sculpting Nanoscale Functional Channels in Complex Oxides Using Energetic Ions and Electrons. *ACS Appl. Mater. Interfaces* **2018**, *10*, 16731−16738.
(40) Burggraaf, A. J.; van Dijk, T.; Verkerk, M. J. Structure and Conductivity of Pyrochlore and Fluorite Type Solid Solutions. *Solid State Ionics* **1981**, *5*, 519−522.
(41) van Dijk, M. P.; de Vries, K. J.; Burggraaf, A. J. Oxygen Ion and Mixed Conductivity in Coumpounds with the Fluorite and Pyrochlore Structure. *Solid State Ionics* **1983**, *9*−*10*, 913−920.
(42) Yuan, F.; Liu, B.; Zhang, Y.; Weber, W. J. Segregation and Migration of the Oxygen Vacancies in the $\sum$3 (111) Tilt Grain Boundaries of Ceria. *J. Phys. Chem. C* **2016**, *120*, 6625−6632.
(43) Aidhy, D. S.; Zhang, Y.; Weber, W. J. Strained Ionic Interfaces: Effect on Oxygen Diffusivity from Atomistic Simulations. *J. Phys. Chem. C* **2014**, *118*, 4207−4212.
(44) McKenna, K.; Shluger, A. The Interaction of Oxygen Vacancies with Grain Boundaries in Monoclinic HfO_2. *Appl. Phys. Lett.* **2009**, *95*, No. 222111.

https://dx.doi.org/10.1021/acsami.0c12250
ACS Appl. Mater. Interfaces 2020, 12, 45558−45563